



**HAL**  
open science

## The electrochemical performance of melt-spun C14-Laves type TiZr-based alloy

Ika Dewi Wijayanti, Live Mølmen, Roman Denys, Jean Nei, Stéphane Gorsse,  
Kwo Young, Matylda Guzik, Volodymyr Yartys

### ► To cite this version:

Ika Dewi Wijayanti, Live Mølmen, Roman Denys, Jean Nei, Stéphane Gorsse, et al.. The electrochemical performance of melt-spun C14-Laves type TiZr-based alloy. *International Journal of Hydrogen Energy*, 2020, 45 (2), pp.527-537. 10.1016/j.ijhydene.2019.02.093 . hal-02435448

**HAL Id: hal-02435448**

**<https://hal.science/hal-02435448>**

Submitted on 9 Jun 2020

**HAL** is a multi-disciplinary open access archive for the deposit and dissemination of scientific research documents, whether they are published or not. The documents may come from teaching and research institutions in France or abroad, or from public or private research centers.

L'archive ouverte pluridisciplinaire **HAL**, est destinée au dépôt et à la diffusion de documents scientifiques de niveau recherche, publiés ou non, émanant des établissements d'enseignement et de recherche français ou étrangers, des laboratoires publics ou privés.

# The electrochemical performance of melt-spun C14-Laves type Ti–Zr-based alloy

Ika Dewi Wijayanti<sup>a,b,c</sup>, Live Mølmen<sup>b</sup>, Roman V. Denys<sup>a</sup>, Jean Nei<sup>d</sup>, Stéphane Gorsse<sup>e,f</sup>, Kwo Young<sup>d</sup>, Matylda N. Guzik<sup>g</sup>, Volodymyr Yartys<sup>a,b,\*</sup>

<sup>a</sup> Department of Battery Technology, Institute for Energy Technology (IFE), Kjeller, Norway

<sup>b</sup> Department of Materials Science and Engineering, NTNU, Trondheim, Norway

<sup>c</sup> Department of Mechanical Engineering, Sepuluh Nopember Institute of Technology (ITS), Surabaya, Indonesia

<sup>d</sup> BASF/Battery Materials–Ovonic, Rochester Hills, USA

<sup>e</sup> CNRS, ICMCB, University of Bordeaux, UMR 5026, Pessac F 33600, France

<sup>f</sup> Bordeaux INP, ENSCBP, Pessac F 33600, France

<sup>g</sup> Department of Physics, University of Oslo, Blindern, Oslo, Norway

## ARTICLE INFO

### Article history:

Received 9 November 2018

Received in revised form

9 February 2019

Accepted 12 February 2019

Available online 8 March 2019

### Keywords:

Ti–Zr based alloy

Metal hydride battery

Rapid solidification

Electrochemical performance

## ABSTRACT

The main objective of the present work is to study the effect of rapid solidification on the electrochemical performance of Zr based Laves type alloy with a nominal composition  $\text{Ti}_{12}\text{Zr}_{21.5}\text{V}_{10}\text{Cr}_{7.5}\text{Mn}_{8.1}\text{Co}_8\text{Ni}_{32.2}\text{Al}_{0.4}\text{Sn}_{0.3}$ . The samples were prepared from the as cast ar melted buttons by melt spinning at different copper wheel rotation speeds of 5, 16.5, 33, and 100 Hz, which are equivalent to linear speeds of 6.3, 21, 41, and 62.8 m s<sup>-1</sup> respectively using a cooling wheel with a diameter of 20 cm. The phase composition and morphology of the ribbons were analyzed by X Ray diffraction (XRD) and scanning electron microscopy (SEM). The microstructural changes of the ribbons induced by the variations in the wheel rotation speed were found to be closely related to the electrochemical performances. High discharge capacities exceeding 400 mAh·g<sup>-1</sup> were achieved for the melt spun samples during the measurements at low current densities. Furthermore, melt spun casting performed at the highest wheel rotation speed of 100 Hz resulted in the best rate performance of the alloy. As this alloy has the smallest crystallite size, this resulted in the shortest H atoms diffusion distances, and thus increased the efficient H diffusion rate and improved the electrochemical performance.

© 2019 Hydrogen Energy Publications LLC. Published by Elsevier Ltd. All rights reserved.

## Introduction

Zr based Laves alloys have become the most promising candidates between the metal hydride (MH) alloys used as negative active electrode materials in the Nickel/Metal Hydride batteries due to their high capacities in storing hydrogen by forming  $\text{AB}_2\text{H}_{3-4}$  hydrides [1–5]. However, poor activation

performance of  $\text{AB}_2$  MH alloys in comparison with that of the commercial  $\text{AB}_5$  MH compositions motivated intensive studies to improve their electrochemical performance [6–8]. Rapid solidification (RS)/rapid quenching is one of the materials processing techniques which produces nanostructured alloys by applying cooling rates exceeding 10<sup>4</sup> K·s<sup>-1</sup> to the molten metal, thus affecting both the phase composition and microstructure of the alloys [9–13]. Both the morphology and

\* Corresponding author. Department of Battery Technology, Institute for Energy Technology (IFE), Kjeller, Norway.  
E mail addresses: [Ika.Dewi.Wijayanti@ife.no](mailto:Ika.Dewi.Wijayanti@ife.no) (I.D. Wijayanti), [Volodymyr.Yartys@ife.no](mailto:Volodymyr.Yartys@ife.no) (V. Yartys).

phase composition resulting from the rapid quenching process can cause variations in the electrochemical performance [14–16]. Particularly, the kinetics of the processes occurring at the metal–electrolyte interface and the rate of hydrogen diffusion within the bulk alloy are changed [17,18]. Therefore, in order to improve the electrochemical performance, the optimized phase structures with fine morphology and an appropriate composition are highly desirable.

In the present study, RS process was performed on the  $Ti_{12}Zr_{21.5}V_{10}Cr_{7.5}Mn_{8.1}Co_8Ni_{32.2}Al_{0.4}Sn_{0.3}$  alloy using different wheel rotation speed rates of 5, 16.5, 33, and 100 Hz. Additions of Cu [19], Fe [20], Zn [21], Si [22], Mo [23], B [24], and Pd [25] to this alloy were studied by BASF group in order to achieve improvements of the high rate dischargeability (HRD) performances. These studies showed that HRD performance improved by adding 2 wt% Pd. By applying the rapid solidification process, thus by achieving its nanostructuring [26,27], we aim at improving the HRD performance of the alloy. Furthermore, the interrelation between the melt spinning rotation speed and the electrochemical properties of multi component Zr based Laves alloys and the corresponding charge discharge mechanism will be presented in this paper. The effects of the variation of the different cooling rates on the crystal structure, microstructure, phase abundance, and electrochemical properties of the rapidly solidified alloys will be reported.

## Experimental methods

Alloy with the composition of  $Ti_{12}Zr_{21.5}V_{10}Cr_{7.5}Mn_{8.1}Co_8Ni_{32.2}Al_{0.4}Sn_{0.3}$  was prepared by induction melting under a protective atmosphere of helium gas by heating up the mixture of the raw materials placed into an  $Al_2O_3$  crucible and holding the formed melt at 1500 °C for 5 min. The composition of the alloy was chosen because of its balanced performances in capacity, high rate dischargeability (HRD), charge retention, and cycle stability, and was previously used as the base material in other studies performed at BASF [24]. The as cast alloy was then used for the castings performed using a SC Edmund Buehler melt spinner accommodated at CNRS/University of Bordeaux (France) at wheel rotation speeds of 5, 16.5, 33, or 100 Hz.

The as cast alloy and four types of melt spun ribbons were mechanically crushed and ground to powder sizes of below 40  $\mu m$  and 40–60  $\mu m$  for the X Ray diffraction (XRD) and electrochemical measurements, respectively. XRD analysis was performed on a Bruker D8 Focus diffractometer using  $Cu K_{\alpha}$  radiation in the  $2\theta$  angle range of 10–90° and with a step size of 0.0015° using a 1 mm slit. Rietveld refinements for the XRD pattern were carried out using the GSAS suite of programs [28] with the EXPGUI interface. A JEOL JSM6320F scanning electron microscope (SEM, Tokyo, Japan) equipped with energy dispersive spectroscopy (EDS) analysis was used to study the phases distribution and their composition.

MH pellet electrodes were prepared by first thoroughly mixing the alloy powder having a particle size of 40–60  $\mu m$  with carbonyl Ni powder with a specific surface area of  $\sim 0.7 m^2 g^{-1}$  in the weight ratio of 1:4, which was then cold

pressed under a pressure of 12 MPa into a 10 mm diameter pellet which was then sandwiched between two Ni foams.

Electrochemical performance was measured using a CT 2001 Land Battery Tester with the three electrode system consisting of a MH alloy working electrode, a sintered  $Ni(OH)_2/NiOOH$  counter electrode, and a Hg/HgO reference electrode using a 9 M KOH aqueous solution as the electrolyte. Galvanostatic method was used to measure the activation and rate performance of MH electrode. MH electrode was charged at a current density of  $100 mA \cdot g^{-1}$  for 5 h followed by a 30 min rest and then discharged at a current density of  $100 mA \cdot g^{-1}$  to a voltage cut-off of 0.7 V against the Hg/HgO reference electrode. After the MH electrode was fully activated, it was charged at a current density of  $100 mA \cdot g^{-1}$  followed by a 30 min rest and discharged at different current densities (0.1–1 C rate) to a voltage cut-off of 0.6 V against the Hg/HgO reference electrode (see Table 1 presenting the details of the electrochemical characterisation experiments performed during the half cell measurements). The discharge rate performances of each sample are shown by calculating the ratio the discharge capacity at the highest current density to the capacity at the lowest current density [29].

## Results and discussion

### Ribbon structure

Morphologies of the ribbons appear to be directly related to the conditions of the Rapid Solidification performed at the University of Bordeaux/CNRS Bordeaux. With increasing wheel rotation speed, RS results in regular changes in width, length and thickness of the produced ribbons (see Fig. 1). Indeed, all dimensions of the ribbons gradually decrease when rotation frequency goes up from 5 to 100 Hz. This is expected as thinner, shorter, and narrower ribbons are anticipated to be produced at higher rotation speeds. Dimensional parameters of the ribbons produced by melt spinning are shown in Table 2.

**Table 1 – Summary of the electrochemical characterisation experiments performed during the half-cell measurements.**

Cycle number	Charge current ( $mA \cdot g^{-1}$ )	Charge time (h)	Discharge current ( $mA \cdot g^{-1}$ )	Discharge cut-off voltage (V)	
1	33	100	5	100	0.7
34	100	5	10	10	0.6
35	100	5	34	34	0.6
36	100	5	68	68	0.6
37	100	5	100	100	0.6
38	100	5	136	136	0.6
39	100	5	169	169	0.6
40	100	5	200	200	0.6
41	100	5	237	237	0.6
42	100	5	271	271	0.6
43	100	5	305	305	0.6

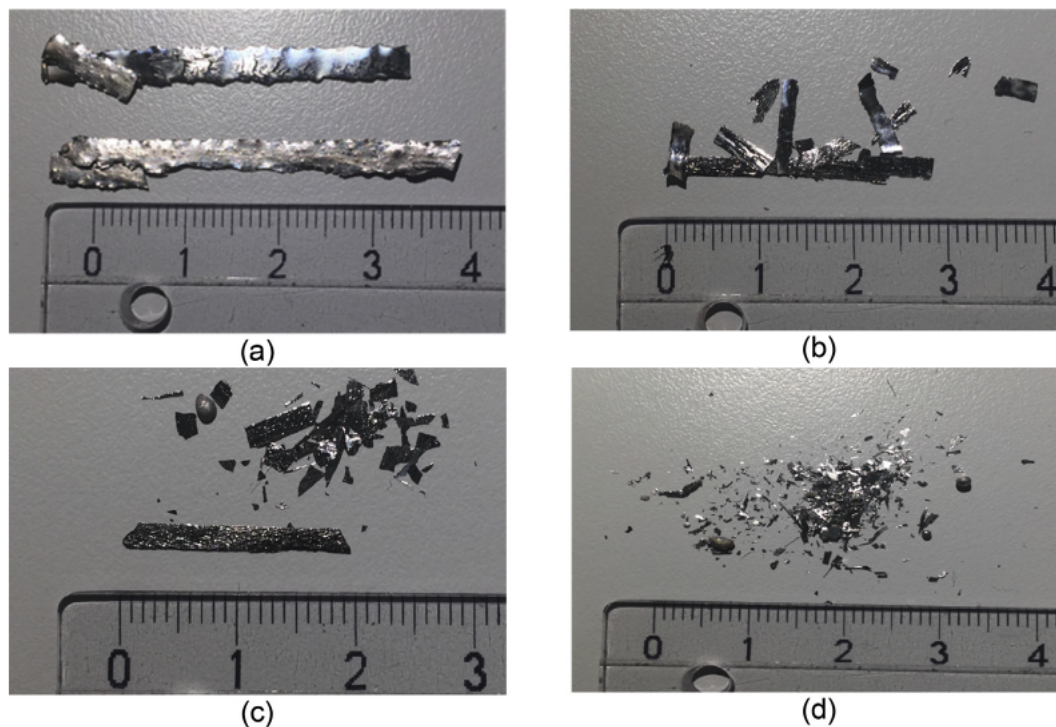


**Fig. 1** – Ribbons produced using melt spinning at different wheel rotation speeds of 5 (a), 16.5 (b), 33 (c), and 100 (d) Hz. Higher solidification rates cause regular changes in width, length, and thickness of the produced ribbons which all gradually decreased when rotation frequency went up from 5 to 100 Hz. Their values change from 0.5, 4.4, and 0.213 mm to 0.1, 0.5, and 0.043 mm, respectively (see [Table 2](#) for the details).

### XRD analysis

XRD patterns of five studied alloys are shown in [Fig. 2](#). All peaks can be fitted to a hexagonal Laves type C14 and a face centered cubic C15 Laves type structures. However, as the C14 phase is the main component with its abundance exceeding 83 wt% for every studied material, in analysis of the crystallite size in GSAS refinements we only considered the related data as contributed by the main C14 phase only.

A typical Rietveld GSAS refinement plot for the as cast sample is presented in [Fig. 3](#), while the data on the unit cell parameters, volumes of the unit cells, crystallite sizes, and phase abundances for the studied samples are given in [Table 3](#). Two conclusions can be made when analyzing the data presented in this Table.

- (a) As the wheel rotation speed increases, the abundance of the C14 phase becomes higher, suggesting that the C14 phase is more likely to form at higher solidification rates

as compared to the C15 phase. This is in agreement with an earlier report [30].

- (b) For the C14 intermetallic the crystallite sizes gradually decrease from the initial 104 nm for the as cast alloy to 21 nm for the sample received by the melt spinning at 100 Hz.

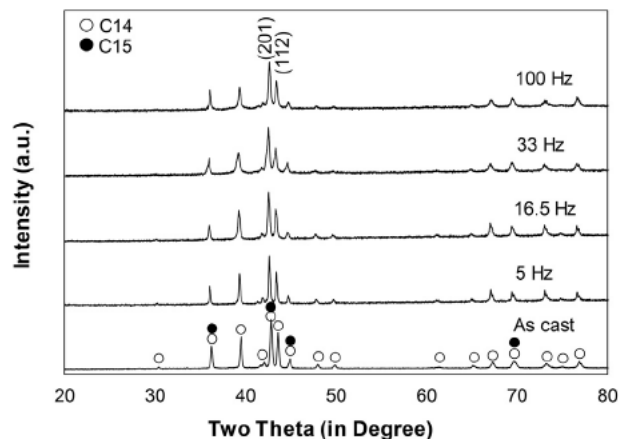


**Fig. 2** – XRD patterns collected using Cu-K $\alpha$  radiation for the as-cast and melt-spun samples with composition  $\text{Ti}_{0.20}\text{Zr}_{0.80}\text{La}_{0.01}\text{Ni}_{1.2}\text{Mn}_{0.70}\text{V}_{0.12}\text{Fe}_{0.12}$  obtained at different wheel rotation speeds of 5, 16.5, 33, and 100 Hz. Two Laves phase intermetallics, C14 (major phase; 83.5 wt%) and C15 (minor phase; 16.5 wt%), were quantitatively identified.

**Table 2** – Characteristics of the ribbons produced by melt spinning.

Sample	Width (mm)	Length (mm)	Thickness (mm)
As cast			
5 Hz	0.5	4.4	0.213
16.5 Hz	0.3	2.9	0.125
33 Hz	0.2	2.0	0.057
100 Hz	0.1	0.1	0.043

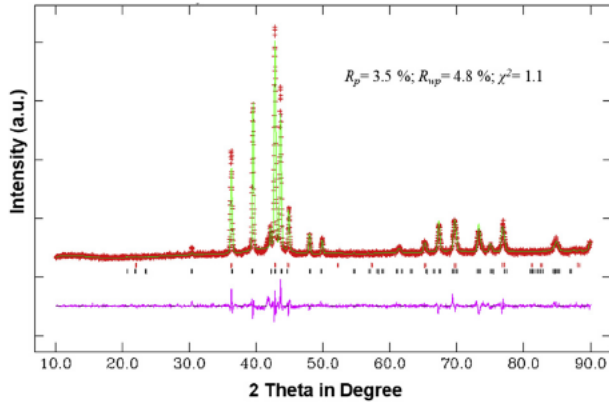


**Fig. 3 – Observed (+), calculated (upper line), and difference (lower line) Rietveld GSAS refinement plots of the XRD pattern of the as-cast sample. The XRD data shows presence of two phases, C14 (83.5 wt%; bottom ticks) and C15 (16.5 wt %; top ticks) intermetallics. Reliability factors are:  $R_p$  3.5%;  $R_{wp}$  4.8%; and  $\chi^2$  1.1.**

As mentioned earlier, due to the small abundance of C15 phase, crystallite size for C15 phases has not been refined.

At the same time, unit cell parameters,  $c/a$  ratios and volumes of the unit cells show only slight variations (1.3% in maximum for the volumes of the C14 Laves phase and 0.6% for the volumes of the C15 phase). These variations are probably related to the small changes in the stoichiometry of the alloys introduced during the melt casting process.

#### SEM/EDS analysis

Microstructures of the alloys were studied by SEM, and their images collected in the backscattered electron (BSE) mode are presented in Fig. 4.

As cast sample shows a formation of the two phase microstructure containing C14 Laves type intermetallic as the main constituent and a secondary C15 intermetallic, with the main phase having a grain size with a length of appr.  $15 \mu\text{m}$  and a width of appr.  $3\text{--}5 \mu\text{m}$  (see Fig. 4).

Casting by rapid solidification significantly and regularly changes the phase composition and morphology of the constituents because of the increasing solidification rate being proportional to the increasing wheel rotation speed.

#### Rapid solidification causes the following changes

- Grain size significantly and gradually decreases with increasing the wheel rotation speed. Indeed, already at a rotation speed of 5 Hz the grain size drops from the initial  $15 \mu\text{m}$  to just approximately  $2 \mu\text{m}$  at 5 Hz and further down to  $900 \text{ nm}$  at 100 Hz.
- Increased rate of RS causes formation of a dendrite microstructure. Dendrites appear in the samples casted at 16.5 Hz and at 33 Hz. The size ( $3 \rightarrow 2 \mu\text{m}$ ) and arm spacing ( $250 \rightarrow 200 \text{ nm}$ ) of the dendritic structure decreases with increasing solidification rate ( $16.5 \rightarrow 33 \text{ Hz}$ ).
- Finally, at 100 Hz rotation speed, the morphology becomes more uniform with a matrix C14 phase composing a core and a secondary C15 phase forming a shell. Large number of nuclei of the main C14 phase is formed in the RS samples due to the higher melting temperature of this intermetallic. When the rotation speed increases, these nuclei do not have enough time to grow and these limitations in the kinetics of growth result in a smaller dendrite sizes and arm spacings. When reaching the highest solidification rate, the matrix and secondary phase compete with each other to firstly nucleate while not always having a sufficient time to grow. By increasing the rotation speed to 100 Hz, a homogeneous structure with a more even distribution of secondary phase in the structure is formed while the dendrite structure is no longer observed.

#### Electrochemical measurements

As shown in Fig. 5, the as cast alloy has the best activation performance among all studied alloys, requiring approximately 10 activation cycles to reach the discharge capacity of close to  $280 \text{ mA} \cdot \text{g}^{-1}$ . All melt spun alloys need more than 15 cycles to be activated, even up to 17 to 20 cycles for a 16.5 Hz speed (Fig. 5 (a)). We assume that the RS process increased the thickness of the native oxide on the MH alloy surface which required extra cycles of charge discharge to be removed. The increase in the C14 phase abundance and a larger amount of the surface oxides in the starting 5 Hz RS alloy caused a more difficult activation of the sample. Similar difficulties in activation were observed for other RS materials. Thirty three cycles were performed for all the melt spun alloys to ensure that the MH electrodes were fully activated and ready for the discharge rate measurements. Among all the melt spun alloys, 100 Hz melt spun alloy showed the fastest activation and

**Table 3 – Crystallographic data, crystallite size and phase abundances for the as-cast and melt-spun samples from the Rietveld GSAS refinements.**

Alloy	C14				Crystallite size, nm	Abundance, wt. %	C15		
	$a, \text{Å}$	$c, \text{Å}$	$c/a$	$V, \text{Å}^3$			$a, \text{Å}$	$V, \text{Å}^3$	Abundance wt. %
As cast	4.9662 (1)	8.0935 (2)	1.6297	172.9 (1)	104	83.5 (4)	7.0037 (3)	343.5 (4)	16.5 (1)
5 Hz	4.9454 (2)	8.0587 (3)	1.6295	170.7 (1)	29	89.3 (4)	6.9888 (1)	341.3 (2)	10.7 (4)
16.5 Hz	4.9594 (2)	8.0800 (5)	1.6292	172.1 (2)	26	94.3 (3)	7.0106 (6)	344.6 (9)	5.7 (3)
33 Hz	4.9563 (4)	8.0761 (8)	1.6294	171.8 (4)	21	84.6 (8)	6.9945 (6)	342.2 (9)	15.4 (2)
100 Hz	4.9660 (4)	8.0906 (8)	1.6291	172.8 (4)	21	83.8 (1)	7.0173 (6)	345.5 (9)	16.2 (3)

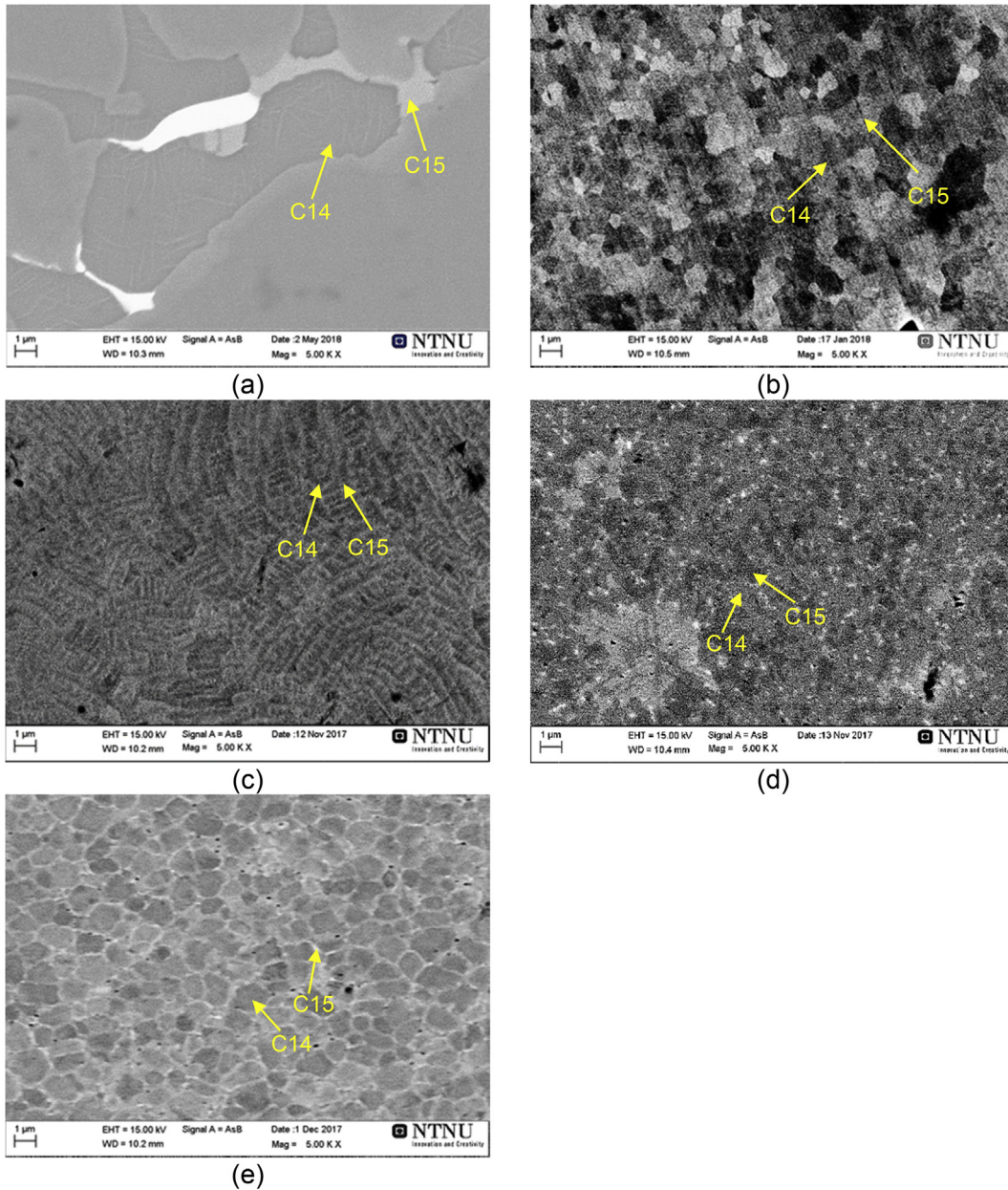


**Fig. 4 – BSE SEM micrographs of as-cast (a) and melt-spun samples produced at different rotation speeds of 5 Hz (b), 16.5 Hz (c), 33 Hz (d), and 100 Hz (e).**

the highest discharge capacity (after 33 charge discharge cycles) of  $237 \text{ mAh}\cdot\text{g}^{-1}$ . This can be due to its optimized microstructure showing a significant refinement, and a rather limited phase segregation as compared to the other melt spun samples.

The discharge rate performances of each sample are presented in Fig. 5 (b). These rate performances were evaluated by calculating high rate dischargeability (HRD) given in Table 4, which presents the ratio of the discharge capacity available at the highest current density of  $304 \text{ mA g}^{-1}$  to the electrochemical capacity at the lowest current density at  $10 \text{ mA g}^{-1}$ . The as cast alloy shows the highest discharge capacity at most applied discharge current densities. The highest discharge capacity at the lowest current density

measurement is observed for the melt spun 16.5 Hz sample. This capacity drops faster during the initial increase in current densities, but the decrease in capacity slows down as the current density increases further indicating that the RS process effectively improves the rate performance at higher current densities. Gradual capacity decrease for the studied alloys with increasing current densities can be observed clearer by analyzing the data of the Table 4. The largest decrease in HRD is found to happen for a 16.5 Hz sample, then followed by 33 Hz and 5 Hz samples. However, this rapid decrease only takes place at lower current densities. As cast sample shows the smallest decrease in the capacity at the beginning, but it becomes more pronounced when the current density increases.

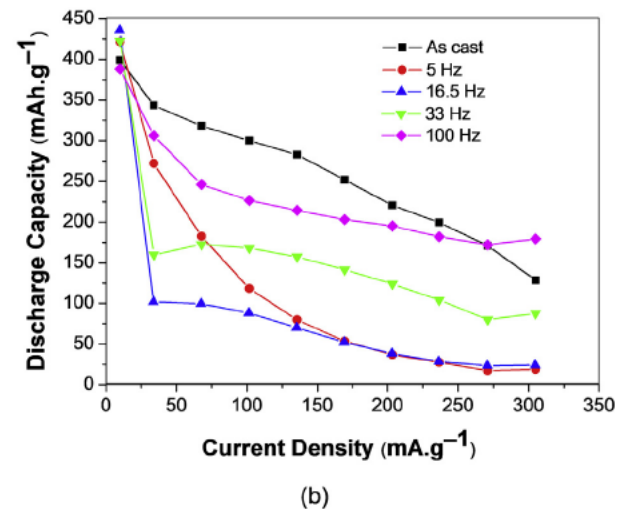
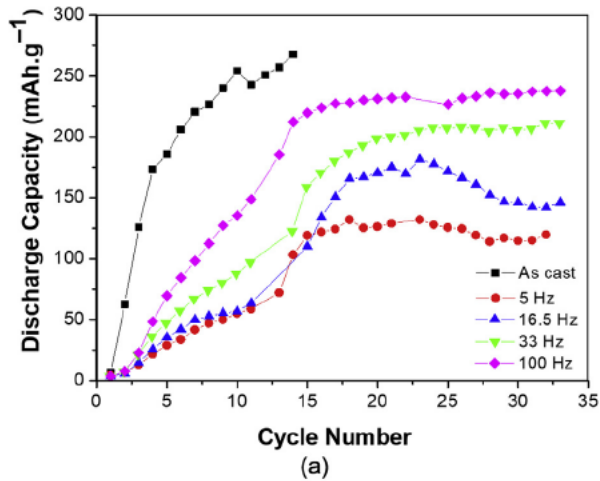


**Fig. 5 – Electrochemical activation on cycling (a) and rate dependence of discharge capacity (b) of the alloys studied in this work. The activation becomes more difficult for the melt-spun samples; however, the best rate performance is achieved at the highest rotation speed of 100 Hz, as can be concluded from its lowest slope.**

We observe evidences that different quenching rates achieved due to the variation of the wheel rotation speed of the melt spinner result in microstructural changes in the alloy

**Table 4 – HRD characteristics of the as-cast and melt-spun samples (%).**

Current density (mA.g <sup>-1</sup> )	As cast	5 Hz	16.5 Hz	33 Hz	100 Hz
10	100	100	100	100	100
34	86	64	23	38	79
68	80	43	23	41	63
100	75	28	20	40	58
136	71	19	16	37	55
169	63	13	12	33	52
200	55	9	9	29	50
237	50	6	7	25	47
271	43	4	5	19	44
304	32	4	6	21	46

which significantly affect the electrochemical performance. Further to the microstructural modifications, the abundance of the C14 and C15 phases also changes as a result of rapid solidification. The ratio C14/C15 plays an important role in electrode performance as C14 phase is favourable for achieving high electrochemical capacity while C15 phase causes high rate performance of the electrode. With increasing the rotation speed, the higher solidification rates are achieved which results in reduced grain sizes of the processed alloy. Lower solidification rates resulting from application of lower wheel rotation speeds (16.5 and 33 Hz) cause formation of dendritic structures and such morphology slows down hydrogen diffusion thus causing inferior rate performance of the battery anodes. Not only slowing down of the hydrogen diffusivity but also a decrease in the surface exchange currents for the dendritic structures were reported earlier in the reference data [31] and were linked to the inferior rate performance of the metal hydride anodes. Thus, forming a homogeneous nano structured metal hydride anode with an optimised ratio C14/C15 which was achieved for the highest applied solidification rate will allow reaching the best electrochemical performance.

The best HRD performance is observed for the 100 Hz sample which is showing only a small drop in the discharge capacity at each step of ramping up of the applied current density during the HRD experiments. This is probably caused by the smallest crystallite sizes observed for this sample resulting in the fastest hydrogen diffusion in the bulk material.

The slight compositional variations and phase structural changes induced by RS process affect the activation and rate performances. The most abundant C14 phase which is less prone to pulverization with smaller amount of the C15 phase present in the melt spun alloy (which undergoes hydride decrepitation faster and more easily) correlates with the poorer activation performance of the C14 predominant alloys. The surface of these alloys should be activated to reach their maximum electrochemical capacity, and a treatment in hot (80 °C) KOH solution is one of the possible options to try. On the other hand, the optimized structure obtained by reaching an appropriate ratio between C14 and C15 phases provides a synergetic effect and improves the rate performance. Moreover, RS process proved to cause a pronounced refinement of the microstructures thus reducing the distance for the hydrogen diffusion and creating a faster hydrogen diffusion paths through the alloy.

## Conclusions

The effect of cooling rate variation during the melt casting of the  $Ti_{12}Zr_{21.5}V_{10}Cr_{7.5}Mn_{8.1}Co_{8}Ni_{32.2}Al_{0.4}Sn_{0.3}$  alloy has been studied. All melt spun samples showed a predominant formation of the C14 Laves type intermetallic phase. Rapid solidification process significantly affects the morphology and microstructure of the alloys. Equiaxed grain structure is formed at a lower rotation speed, while the dendritic structures solidify at higher rotation speeds, and finally the dendritic structure vanished and equiaxed grains with the phase segregation at the grain boundaries are observed at the highest rotation speed. The discharge rate performances improved with the rapid solidification process and were the best at the highest applied

cooling rate achieved at 100 Hz. This phenomenon is believed to be due to the optimized structure obtained by reaching an appropriate ratio between C14 and C15 phases providing a synergetic effect and improving the rate performance.

## Acknowledgement

This work was supported by Norwegian Research Center on Zero Emission Energy Systems for Transport (MoZEES). We thank CNRS/University of Bordeaux and Prof. Jean Louis Bobet for the availability of the laboratory facilities for the rapid solidification process, and BASF Ovonic Rochester Hills, USA for the access to their research laboratories during the work on this project. Ika Dewi Wijayanti received a fellowship from Indonesia Endowment fund for Education (LPDP) to perform a PhD research project at NTNU/IFE in Norway.

## REFERENCES

- [1] Yartys V, Noreus D, Latroche M. Metal hydrides as negative electrode materials for NiMH batteries. *Appl Phys A* 2016;122:43.
- [2] Young K H, Nei J, Wan C, Denys R, Yartys V. Comparison of C14 and C15 predominated AB<sub>2</sub> metal hydride alloys for electrochemical applications. *Batteries* 2017;3:22.
- [3] Young K H, Koch JM, Wan C, Denys RV, Yartys VA. Cell performance comparison between C14 and C15 predominated AB<sub>2</sub> metal hydride alloys. *Batteries* 2017;3:29.
- [4] Young K H, Nei J. The current status of hydrogen storage alloy development for electrochemical applications. *Materials* 2013;6:4574–608.
- [5] Fetcenko MA, Ovshinsky SR, Reichman B, Young K, Fierro C, Koch J, et al. Recent advances in NiMH battery technology. *J Power Sources* 2007;165:544–51.
- [6] Tan S, Shen Y, Onur Şahin E, Noréus D, Öztürk T. Activation behavior of an AB<sub>2</sub> type metal hydride alloy for NiMH batteries. *Int J Hydrog Energy* 2016;41:9948–53.
- [7] Miao H, Gao M, Liu Y, Lin Y, Wang J, Pan H. Microstructure and electrochemical properties of Ti–V based multiphase hydrogen storage electrode alloys Ti<sub>0.8</sub>Zr<sub>0.2</sub>V<sub>2.7</sub>Mn<sub>0.5</sub>Cr<sub>0.8-x</sub>Ni<sub>1.25</sub>Fe<sub>x</sub> (x=0.0–0.8). *Int J Hydrog Energy* 2007;32:3947–53.
- [8] Liu Y, Pan H, Gao M, Wang Q. Advanced hydrogen storage alloys for Ni/MH rechargeable batteries. *J Mater Chem* 2011;21:4743–55.
- [9] Suwarno S, Solberg JK, Maehlen JP, Krogh B, Børresen BT, Ochoa Fernandez E, et al. Microstructure and hydrogen storage properties of as cast and rapidly solidified Ti rich Ti–V alloys. *Trans Nonferrous Metals Soc China* 2012;22:1831–8.
- [10] Wu Y, Lototsky MV, Solberg JK, Yartys VA. Microstructural evolution and improved hydrogenation–dehydrogenation kinetics of nanostructured melt spun Mg–Ni–Mm alloys. *J Alloy Comp* 2011;509:S640–5.
- [11] Wu Y, Han W, Zhou SX, Lototsky MV, Solberg JK, Yartys VA. Microstructure and hydrogenation behavior of ball milled and melt spun Mg–10Ni–2Mm alloys. *J Alloy Comp* 2008;466:176–81.
- [12] Wu Y, Solberg JK, Yartys VA. The effect of solidification rate on microstructural evolution of a melt spun Mg–20Ni–8Mm hydrogen storage alloy. *J Alloy Comp* 2007;446–447:178–82.
- [13] Nwakwu CC, Holm T, Denys RV, Hu W, Maehlen JP, Solberg JK, et al. Effect of magnesium content and quenching rate on the phase structure and composition of rapidly solidified La<sub>2</sub>MgNi<sub>9</sub> metal hydride battery electrode alloy. *J Alloy Comp* 2013;555:201–8.
- [14] Zhang Y, Shang H, Li Y, Hou Z, Qi Y, Guo S. Structure and electrochemical hydrogen storage behaviors of RE–Mg–Ni–Co–Al based AB<sub>2</sub> type alloys prepared by melt spinning. *J Alloy Comp* 2017;699:378–85.
- [15] Zhang Y, Ren H, Li B, Guo S, Pang Z, Wang X. Electrochemical hydrogen storage characteristics of nanocrystalline and amorphous Mg<sub>20</sub>Ni<sub>10-x</sub>Co<sub>x</sub> (x=0–4) alloys prepared by melt spinning. *Int J Hydrog Energy* 2009;34:8144–51.
- [16] Zhang Y, Cai Y, Zhao C, Zhai T, Zhang G, Zhao D. Electrochemical performances of the as melt La<sub>0.75-x</sub>M<sub>x</sub>Mg<sub>0.25</sub>Ni<sub>3.2</sub>Co<sub>0.2</sub>Al<sub>0.1</sub> (M=Pr, Zr; x=0, 0.2) alloys applied to Ni/metal hydride (MH) battery. *Int J Hydrog Energy* 2012;37:14590–7.
- [17] Zhang SK, Shu KY, Lei YQ, Lü GL, Wang QD. Effect of solidification rate on the phase structure and electrochemical properties of alloy Zr<sub>0.7</sub>Ti<sub>0.3</sub>(MnVNi)<sub>2</sub>. *J Alloy Comp* 2003;352:158–62.
- [18] Zhang Y, Li B, Ren H, Wu Z, Dong X, Wang X. Investigation on structures and electrochemical characteristics of the as cast and quenched La<sub>0.5</sub>Ce<sub>0.2</sub>Mg<sub>0.3</sub>Co<sub>0.4</sub>Ni<sub>2.6-x</sub>Mn<sub>x</sub> (x=0–0.4) electrode alloys. *J Alloy Comp* 2008;461:591–7.
- [19] Young K H, Ouchi T, Huang B, Reichman B, Fetcenko MA. Studies of copper as a modifier in C14 predominated AB<sub>2</sub> metal hydride alloys. *J Power Sources* 2012;204:205–12.
- [20] Young K H, Ouchi T, Huang B, Reichman B, Fetcenko MA. The structure, hydrogen storage, and electrochemical properties of Fe doped C14 predominating AB<sub>2</sub> metal hydride alloys. *Int J Hydrog Energy* 2011;36:12296–304.
- [21] Young K, Ouchi T, Lin X, Reichman B. Effects of Zn addition to C14 metal hydride alloys and comparisons to Si, Fe, Cu, Y, and Mo additives. *J Alloy Comp* 2016;655:50–9.
- [22] Young K H, Ouchi T, Huang B, Reichman B, Blankenship R. Improvement in 40 C electrochemical properties of AB<sub>2</sub> metal hydride alloy by silicon incorporation. *J Alloy Comp* 2013;575:65–72.
- [23] Young K H, Ouchi T, Huang B, Reichman B, Fetcenko MA. Effect of molybdenum content on structural, gaseous storage, and electrochemical properties of C14 predominant AB<sub>2</sub> metal hydride alloys. *J Power Sources* 2011;196:8815–21.
- [24] Chang S, Young K H, Ouchi T, Nei J, Wu X. Effects of Boron incorporation in a V containing Zr based AB<sub>2</sub> metal hydride alloy. *Batteries* 2017;3:36.
- [25] Young K H, Ouchi T, Nei J, Chang S. Increase in the surface catalytic ability by addition of Palladium in C14 metal hydride alloy. *Batteries* 2017;3:26.
- [26] Zhang Y, Zhao C, Yang T, Shang H, Xu C, Zhao D. Comparative study of electrochemical performances of the as melt Mg<sub>20</sub>Ni<sub>10-x</sub>M<sub>x</sub> (M=None, Cu, Co, Mn; x=0, 4) alloys applied to Ni/metal hydride (MH) battery. *J Alloy Comp* 2013;555:131–7.
- [27] Zhang Y, Liu Z, Li B, Ma Z, Guo S, Wang X. Structure and electrochemical performances of Mg<sub>2</sub>Ni<sub>1-x</sub>Mn<sub>x</sub> (x=0–0.4) electrode alloys prepared by melt spinning. *Electrochim Acta* 2010;56:427–34.
- [28] Larson AC, Von Dreele RB. General structure analysis system (GSAS), Los Alamos national laboratory report LAUR 86 748. 2004.
- [29] Young K, Ouchi T, Liu Y, Reichman B, Mays W, Fetcenko M. Structural and electrochemical properties of Ti<sub>2</sub>Zr<sub>7-x</sub>Ni<sub>10</sub>. *J Alloy Comp* 2009;480:521–8.
- [30] Stein F, Palm M, Sauthoff G. Structure and stability of Laves phases part II—structure type variations in binary and ternary systems. *Intermetallics* 2005;13:1056–74.
- [31] Young K, Young M, Ouchi T, Reichman B, Fetcenko MA. Improvement in high rate dischargeability, activation, and low temperature performance in multi phase AB<sub>2</sub> alloys by partial substitution of Zr with Y. *J Power Sources* 2012;215:279–87.